A&A, 714, A515 (2026)
https://doi.org/10.1051/0004-6361/202659702
© The Authors 2026

Astronomy & Astrophysics

Two-body relaxation in the EMRI-TDE disk model for quasi-periodic eruptions

Chiara Maria Allievi[1,⋆], Luca Broggi[1,2], Alberto Sesana[1,2], and Matteo Bonetti[1,2,3]

[1] Dipartimento di Fisica "G. Occhialini", Università degli Studi di Milano-Bicocca, Piazza della Scienza 3, I-20126 Milano, Italy
[2] INFN, Sezione di Milano-Bicocca, Piazza della Scienza 3, I-20126 Milano, Italy
[3] INAF – Osservatorio Astronomico di Brera, Via Brera 20, I-20121 Milano, Italy

Received 4 March 2026 / Accepted 30 August 2026

ABSTRACT

Quasi-periodic eruptions (QPEs) are luminous bursts of soft X-rays that were recently discovered in galactic nuclei. They repeat on timescales of hours to weeks and are superimposed on an otherwise stable quiescent X-ray level, consistent with emission from a radiatively efficient accretion flow around relatively low-mass massive black holes (MBHs). Although their physical origin is still debated, their quasi-periodicity naturally arises within the "impact model", in which the X-ray bursts are generated by the interaction between a stellar black hole (sBH) or a star in a close orbit around the central MBH and the accretion disk formed by a tidal disruption event (TDE). While this model is consistent with the phenomenology of QPEs, it remains unclear whether such specific physical configurations are sufficiently common to explain the observed QPE number density. We present the first end-to-end quantitative calculation of the expected QPE rate and abundance within the framework of the impact model. For this purpose, we combined the rates of TDEs and extreme mass-ratio inspirals (EMRIs) around MBHs spanning a range of masses. We employed the public code PHASEFLOW to simulate seven systems with MBH masses between $10^5\,M_\odot$ and $10^8\,M_\odot$, each surrounded by a three-component population: one composed of $1\,M_\odot$ stars, and two consisting of sBHs with masses of $10\,M_\odot$ and $40\,M_\odot$. Based on the emission constraints available in the literature, we restricted our analysis to sBH EMRIs on prograde orbits with eccentricity $e < 0.5$ and inclination $i < 20°$ with respect to the accretion disk. For stellar EMRIs, we instead required the star to avoid tidal disruption, which set the constraints. We find that the predicted QPE number density spans the range $10^{-12}\,\mathrm{Mpc}^{-3}$ to $10^{-6}\,\mathrm{Mpc}^{-3}$, depending on the assumed orbital period interval and on the adopted eccentricity and inclination thresholds. Stellar EMRIs can generate QPEs with number densities comparable to those inferred from current observations. In contrast, imposing the orbital constraints required for the sBH channel significantly suppresses the number of observable events, resulting in abundances approximately three orders of magnitude lower than those in the stellar case. If the eccentricity and inclination constraints are relaxed, sBH-driven QPEs become compatible with the lower bound of the observationally inferred range.

Key words. accretion, accretion disks – black hole physics – gravitational waves – methods: numerical – binaries: general

1. Introduction

X-ray quasi-periodic eruptions (QPEs) are an extreme and rather enigmatic phenomenon identified in the last decade (Miniutti et al. 2019). They have luminosities of up to $10^{43}\,\mathrm{erg\,s^{-1}}$, a typical duration of one or a few hours, and recurrence timescales around ten times longer than their durations. These eruptions are associated with rapid spectral transitions between cold and warm phases in the accretion flow around a low-mass massive black hole (MBH).

Since their discovery, QPEs have been observed in the nuclei of eleven other galaxies (Giustini et al. 2020; Chakraborty et al. 2021; Arcodia et al. 2021; Quintin et al. 2023; Arcodia et al. 2024; Nicholl et al. 2024; Guolo et al. 2024; Chakraborty et al. 2025; Hernández-García et al. 2025).

The nature of the host galaxy is still under investigation. Half of them may be relatively low-mass post-starburst galaxies, a population that might be a preferential host for observed tidal disruption events (TDEs), (Miniutti et al. 2019; Chakraborty et al. 2021; Giustini et al. 2020; Arcodia et al. 2021; Guolo et al. 2024). Despite very little X-ray obscuration, none of the QPE galaxies show the typical optical or UV broad emission lines associated with unobscured, type I active galactic nuclei (AGNs), although the observed narrow emission lines suggest the presence of an ionizing AGN-like continuum (Wevers et al. 2022), possibly suggesting past AGN activity.

The physical mechanism producing QPEs is the subject of active debate. A first class of models associates QPEs with intrinsic instabilities in the accretion flow around the central MBH. In this scenario, eruptions arise from recurrent transitions in the inner disk, for instance due to thermal-viscous or radiation-pressure instabilities, which can drive repeated cycles of enhanced accretion and soft X-ray emission (Pan et al. 2022; Śniegowska et al. 2023; Kaur et al. 2023). These models naturally connect QPEs to the physics of accretion disks; however, because the instabilities are generated internally, they do not provide a robust external clock capable of enforcing the strict repeating periodicity observed in most QPE sources. As a result, they may struggle to reproduce features such as alternating long–short recurrence intervals and strong–weak amplitude patterns unless additional modulating physics is introduced.

A second class of models invokes the interaction between an accretion disk and a secondary object orbiting the MBH. In disk-impact models, a star or a stellar-mass black hole (sBH) on a bound orbit periodically crosses the disk. Each crossing shocks and strips part of the disk gas, producing expanding optically thick bubbles that cool and radiate in

⋆ Corresponding author: c.allievi6@campus.unimib.it

Open Access article, published by EDP Sciences, under the terms of the Creative Commons Attribution License (https://creativecommons.org/licenses/by/4.0), which permits unrestricted use, distribution, and reproduction in any medium, provided the original work is properly cited.
This article is published in open access under the Subscribe to Open model. Subscribe to A&A to support open access publication.

soft X-rays, giving rise to recurrent eruptions on a timescale related to the orbital period of the secondary (Dai et al. 2010; Xian et al. 2021; Linial & Metzger 2023; Franchini et al. 2023). In this framework, the disk may be supplied by a pre-existing, weak, AGN-like accretion flow or by the debris of a recent TDE. The latter possibility is particularly relevant because it links QPEs to transient disks formed after stellar disruptions (Linial & Metzger 2023; Kaur et al. 2023). Two known QPE sources show long-term decays in quiescent luminosity consistent with TDEs (Miniutti et al. 2023; Arcodia et al. 2024), and four observed TDEs have produced X-ray flares resembling individual QPE eruptions (Chakraborty et al. 2021; Quintin et al. 2023; Nicholl et al. 2024; Chakraborty et al. 2025). Although TDEs are expected to occur in only about one out of every 10^4 galaxies, their detection in roughly half of the galaxies hosting QPEs suggests that such a connection might not be coincidental.

In this work we focus on the model in which the interaction between a star or an sBH and a TDE accretion disk gives rise to QPEs. Specifically, we build on the results of Franchini et al. (2023), who model successive passages of QPEs within the sBH extreme mass-ratio inspiral (EMRI)–TDE disk framework, and we extend this model by also considering interactions involving stellar EMRIs. We present the derivation of the number density of QPEs in the Universe, referred to as the QPE volumetric abundance, to assess whether our theoretical predictions are consistent with observational estimates.

The paper is organized as follows. In Sect. 2 we review the aspects of the theory relevant to our model of the QPE origin and present the theoretical reasoning behind the computation of the cosmic QPE volumetric abundance. In Sect. 3 we present the simulations of the nuclear star clusters (NSCs) that we considered and the implementation of the computation of the EMRI and TDE rates. In Sect. 4 we explain the calculations behind the cosmic QPE volumetric abundance. Finally, in Sect. 5 we present the results of our work, which we discuss in Sect. 6, before drawing our conclusions in Sect. 7.

2. Disk impact model

In the model we consider, QPEs are produced by the collisions between a TDE accretion disk and a compact orbiter[1] (CO). Given the scale of the system, the orbiter typically undergoes an EMRI around a MBH at the center of a galaxy (see Fig. 1), as its motion is dominated by gravitational-wave (GW) emission. When the orbiter pierces the accretion disk, it strips some of its mass, which then expands to form two bubbles: one on each side of the impact. Because of the expansion, the bubbles cool until they become optically thin and start emitting electromagnetic radiation. Since EMRIs can have semimajor axes entirely within the radial extent of the TDE disk, they periodically intersect the disk with a recurrence timescale that can match the observed timing of QPE bursts, including small differences between subsequent passages (Franchini et al. 2023).

As sBHs do not have a proper physical surface, their cross section with the gas in the disk is dynamically set as the Bondi radius, i.e., $R = GM/(v_{\rm rel}^2 + v_{\rm sound}^2)$ (Bondi 1952). This imposes constraints on the EMRI orbit to reproduce the luminosities of QPEs; specifically, the relative velocity between the sBH and the gas should be small enough to produce a sufficiently large radius. This translates into constraints on the orbital parameters, namely, the orbital eccentricity e and the inclination i of the orbital plane with respect to the disk: the eccentricity must be small to moderate ($e \lesssim 0.5$) and the inclination must be small ($i \lesssim 20°$) (Franchini et al. 2023; Chakraborty et al. 2024).

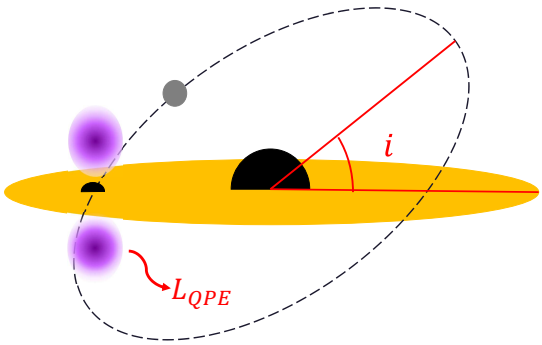


Fig. 1. Schematic representation of the QPE disk-impact model. The large black dot at the center represents the MBH, the small gray dot represents the compact orbiter (either an sBH or a star), the yellow area represents the TDE accretion disk, and the dashed line represents the EMRI trajectory. The angle between the disk and the EMRI orbital plane is the inclination i. The violet bubbles represent the stripped mass that expands both above and below the disk after the impact. Once the bubbles become optically thin, they emit electromagnetic radiation ($L_{\rm QPE}$)

If the orbiter is a main-sequence star, the impact radius is naturally set by the physical radius of the star. Therefore, the only constraint on the orbital properties arises from the stellar structure: the pericenter distance r_p of the EMRI must be larger than the tidal radius r_t, within which the star is torn apart by the tidal field of the MBH. This requires $e < 1 - r_t/a$.

We estimated the abundance of QPE sources in the galactic population starting from the expected number of EMRI-TDE disk pairs in a single galactic nucleus. We assumed that the compact orbiter was in place because of the combined effect of two-body relaxation and GW emission. In fact, weak scatterings can deflect orbiters onto low-angular-momentum orbits, where GWs emitted at periastron bind them to the central MBH, initiating the slow, GW-driven, adiabatic inspiral defining an EMRI.

The number of compact orbiters, $N_{\rm CO}$, in the GW-dominated region is estimated as the product of the rate at which orbiters enter this region of phase space and the coalescence time; this number must account for eccentricity and inclination constraints. The number of TDE disks, $N_{\rm disk}$, expected around the MBH is estimated as the product of the stellar disruption rate and the disk lifetime. The product $N_{\rm CO} \times N_{\rm disk}$ gives the expected number of potential QPE sources in a given galactic nucleus. As this number is usually smaller than unity, we interpreted it as the probability of observing an active QPE source in a galactic nucleus.

2.1. TDEs and EMRIs from two-body relaxation

Dynamical interactions within NSCs can drive stellar objects onto very tight orbits around the central MBH. Through this mechanism, some objects are driven either to plunge directly into the MBH, enter an EMRI phase, or, if they are not compact enough to survive, undergo a TDE. Specifically, the finite number of objects in NSCs induces small deviations from the smooth average potential of the system. As a consequence, the orbital parameters of a stellar object undergo Brownian motion

[1] By "compact orbiters", we mean every object around the SMBH outside its tidal disruption radius or its loss cone.

known as two-body relaxation. The leading effect is the accumulation of distant two-body encounters between the considered stellar object and the other objects. For the entire stellar population, the distribution of orbital parameters, which in spherical symmetry can be identified with specific energy and specific angular momentum, can be shown to evolve according to a diffusion-advection equation (the orbit-averaged Fokker-Planck equation). Its coefficients are determined by the dynamics of two-body relaxation (Spitzer 1987).

The Fokker-Planck equation can be modified to account for disruptive processes such as tidal disruptions or gravitational captures according to the loss cone theory[2]. Loss cone phenomena are included by assuming an instantaneous disruption at the pericenter when it is smaller than a critical value $r_{\rm LC}$, which can be treated with modified boundary conditions for the equation (Cohn & Kulsrud 1978).

The Brownian motion of stars in angular momentum is generally faster than that in energy (especially for very eccentric orbits); an approximate description of relaxation is based on decoupling the two processes. One can use a simplified evolution equation for the distribution in energy (the ergodic Fokker-Planck equation) and assume a relaxed profile in angular momentum at any instant. This angular-momentum profile is generally approximated by the nearly radial, steady-state profile induced by loss cone disruptions at fixed energy (Cohn 1979; Merritt 2013; Vasiliev 2017; Stone et al. 2020).

2.1.1. TDEs and their disks

The MBH can tidally disrupt a star if it enters a critical radius (Hills 1975; Rees 1988; Phinney 1989). This distance is known as the tidal disruption radius r_t, and encloses the region in space where the tidal forces of the MBH overcome the self-gravity of a star, so that the latter is ripped apart. For a star of mass $M_\star$ and radius $R_\star$ it can be estimated as (Hills 1975)

$$r_t = \eta_\star \left(\frac{M_\bullet}{M_\star}\right)^{1/3} R_\star \tag{1}$$

where the form factor $\eta_\star \simeq 1$ depends on the internal structure of the star and possibly the eccentricity of the orbit. For stars, we assume loss cone events to happen with $r_{\rm LC} = r_t$, with $\eta_\star = 1$.

We assumed that every star penetrating the tidal radius was disrupted by the MBH and formed an accretion disk. Simulations show that the stellar debris of a TDE follows a range of trajectories, with some of the material becoming unbound and escaping. Conversely, the bound debris returns to the pericenter on highly eccentric orbits, possibly self-interacting because of relativistic precession and orbital dynamics. These collisions dissipate energy and facilitate the circularization of the debris, leading to the gradual formation of the accretion disk (Dai et al. 2010; Shen & Matzner 2014; Bonnerot & Lu 2020; Curd 2021). This disk is the central engine that powers the long-term electromagnetic emission of a TDE, and emits radiation across multiple wavelengths as the material spirals inward and is accreted onto the black hole (Lodato & Rossi 2010; Lodato et al. 2015; Mummery & Balbus 2020). We assumed a disk lifetime $\tau_{\rm disk}$ of 10 yr, consistent with estimates from viscous disk-evolution models for TDE debris disks (Cannizzo et al. 1990; Montesinos Armijo & de Freitas Pacheco 2011; Piro & Mockler 2025).

2.1.2. EMRIs

An EMRI can form when two-body relaxation brings a stellar object into an orbit so close to the central MBH that the emission of GWs dominates over relaxation and drives the object to coalescence. This transition is governed by the two-body relaxation timescale, $t_{\rm rlx}$, defined as the time required for the squared angular momentum, J^2, of an orbit to change by an amount of the order of itself. By defining eccentricity as $J^2/J_c^2 \equiv 1 - e^2$, where $J_c(E)$ is the angular momentum of the circular orbit with energy E, this gives

$$t_{\rm rlx} = \frac{1 - e^2}{\mathcal{D}(E)}, \tag{2}$$

where $\mathcal{D}$ is the diffusion coefficient determined by two-body relaxation and depends only on the orbital energy E. We opted for this definition of the eccentricity e as it extends the Keplerian estimate to non-elliptical orbits influenced by the stellar potential.

To estimate the timescale of GW emission, we considered the shorter of the times required to change $1 - e^2$ and a. The shorter timescale is always $-a/\dot{a}_{\rm GW}$, which, for the typically eccentric loss-cone orbits, can be estimated as (Peters 1964)

$$t_{\rm GW} = \frac{12\sqrt{2}}{85} \frac{c^5}{G^3 M_\bullet^2 M_{\rm CO}} a^4 (1 - e)^{7/2} \tag{3}$$

where we assumed that $M_{\rm CO} \ll M_\bullet$. The dynamics of stellar objects can be described by delimiting two regions in the $(1-e, a)$ plane (see Fig. 2):

(i) the region of stochastic evolution, where $t_{\rm rlx} < t_{\rm GW}$ and the orbital evolution is dominated by two-body encounters;

(ii) the GW-dominated region, where $t_{\rm GW} < t_{\rm rlx}$, and the orbital evolution is dominated by the emission of GWs. Here, the evolution becomes increasingly deterministic as the CO's orbit shrinks.

Since the relaxation for eccentric orbits changes $1 - e^2$ faster than a, objects in the region dominated by two-body relaxation are slowly pushed, approximately at fixed a, to pericenters $r_p < r_{\rm cap}$, resulting in gravitational captures. The value

$$r_{\rm cap} = 8\, G M_\bullet / c^2 = 3.8 \times 10^{-13}\ {\rm pc} \times (M_\bullet / M_\odot) \tag{4}$$

corresponds, for very eccentric orbits, to the angular momentum of the geodesics entering the horizon of the MBH (Merritt 2013). When including gravitational-wave emission, it is possible to quantify the fraction of stellar objects that enter $r_{\rm cap}$ directly (known as direct plunges) and those that instead enter the GW-dominated region (thus forming an EMRI). To a good approximation, one can assume $r_{\rm LC} = r_{\rm cap}$, and classify all captures with semimajor axes larger than a critical value a_c as direct plunges and those with smaller semimajor axes as EMRIs (Hopman & Alexander 2005; Bar-Or & Alexander 2016). This picture fails for $M_\bullet \lesssim 3 \times 10^5\, M_\odot$, as EMRIs can form with a large semimajor axis due to abrupt emission of GWs at periastron (known as cliffhangers, see Qunbar & Stone 2024; Mancieri et al. 2025). However, cliffhangers tend to be very eccentric and are unlikely to contribute significantly to the QPE population due to eccentricity constraints, as we discuss later (Mancieri et al. 2026). The critical semimajor axis can be estimated as the intersection between the line corresponding to

[2] The name loss cone comes from the shape spanned by the velocity vectors that, at a given location in space, are tangent to orbits penetrating within a certain distance. The distance enclosing orbits leading to disruptions, or losses, is known as the loss cone radius.

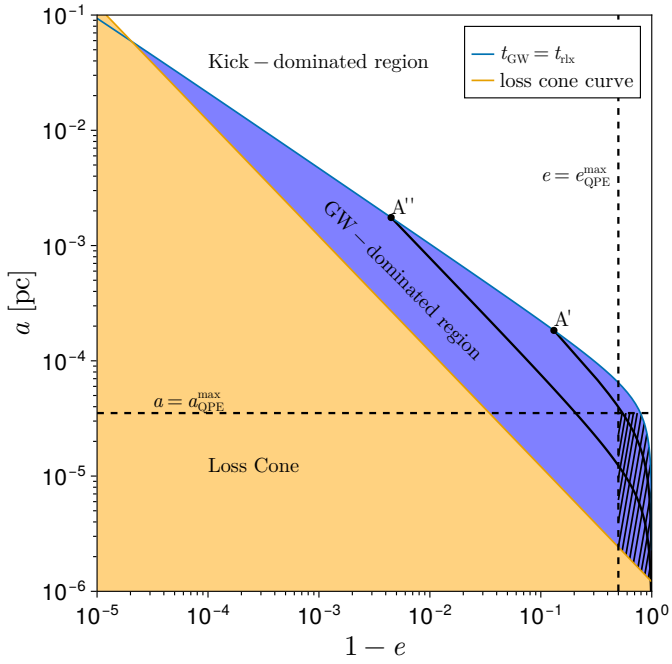


Fig. 2. Trajectories of EMRIs dominated by GW emission. In the blue region, the gravitational-wave timescale t_{GW} is shorter than the relaxation timescale t_{rlx}; the orange area encloses plunging orbits; and the white area encloses orbits dominated by two-body relaxation. The shaded area encloses observable QPEs, which are determined in our model by two parameters: the maximum semimajor axis a^{max}_{QPE} (horizontal dashed) and the maximum eccentricity e^{max}_{QPE} (vertical dashed). The black curves show the trajectories of sBHs that form EMRIs from points A′and A″and become observable QPEs. In this case, $M_\bullet = 3 \times 10^6\, M_\odot$, $M_{CO} = 40\, M_\odot$.

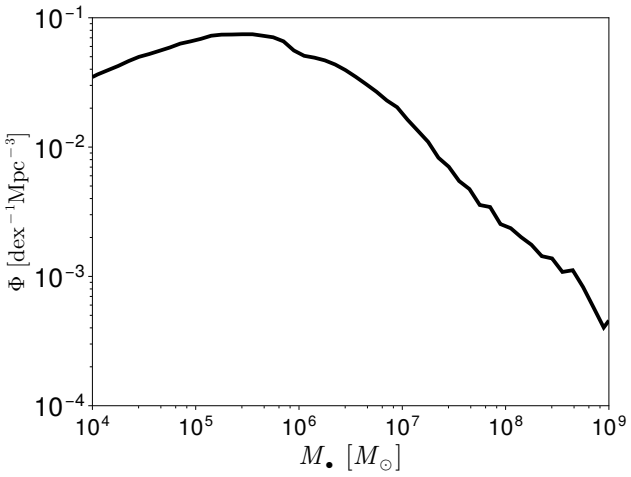


Fig. 3. Black hole mass function Φ used in this work (from Izquierdo-Villalba et al. 2024).

$r_p = r_{cap}$ and the line $t_{rlx} = t_{GW}$ (cf. Fig. 2). We considered nuclei such that $r_t > r_{cap}$, so that stellar EMRIs were disrupted rather than being directly swallowed by the MBH.

2.2. QPE abundance

We estimate the number of active QPEs per galaxy at any instant t as $N_{QPE} = N_{disk}\, N_{CO}$[3]. To express N_{QPE} in terms of EMRI and TDE rates, we considered an observation that began at time t and lasted Δt_{obs}. During the observation time, we see all the disks produced by disruptions that occurred between $t - \tau_{disk}$ and $t + \Delta t_{obs}$. Similarly, the orbiter must be on an EMRI formed between $t - t_{coal}$ and $t + \Delta t_{obs}$[4], where t_{coal} is the time required for the sBH to coalesce or, when considering stellar EMRIs, the time required for a star to reach its tidal disruption radius. Since EMRIs are formed along the curve $t_{rlx} = t_{GW}$ and have different coalescence times, for each type of orbiter we introduced the average coalescence time $\bar{t}_{coal} = N^{tot}_{EMRI}/\Gamma_{EMRI}$.

We assumed that the EMRI rate, Γ_{EMRI}, and the TDE rate, Γ_{TDE}, did not change significantly over the timescales considered, so that $\dot{\Gamma}_{TDE}\, \tau_{disk} \ll \Gamma_{TDE}$ and $\dot{\Gamma}_{EMRI}\, t_{coal} \ll \Gamma_{EMRI}$. We also introduced the QPE selection factor, $\mu^{T,e,i}$, which is the fraction of compact orbiters with T, e and i compatible with detectable QPEs:

$$\mu^{T,e,i} = \frac{N_{CO}}{N^{tot}_{EMRI}}\,. \tag{5}$$

The number of observed QPEs is

$$\begin{aligned} N^{obs}_{QPE} &= N_{disks}\, N_{CO} \\ &= \int_{-\tau_{disk}}^{\Delta t_{obs}} dt'\, \Gamma_{TDE} \times \int_{-t_{coal}}^{\Delta t_{obs}} dt'\, \Gamma_{CO} \\ &\simeq \Gamma_{TDE}\, \Gamma_{CO}\, (\Delta t_{obs} + \tau_{disk})\, (\Delta t_{obs} + t_{coal}) \\ &= \Gamma_{TDE}\, \tau_{disk}\, \Gamma_{EMRI}\, \mu^{T,e,i}\, \bar{t}_{coal} \\ &\quad + \Gamma_{TDE}\, \Gamma_{EMRI}\, \mu^{T,e,i}\, (\tau_{disk} + \bar{t}_{coal})\, \Delta t_{obs} + O\left(\Delta t^2_{obs}\right). \end{aligned} \tag{6}$$

We identify the first term as the number of QPEs that were active at time t, and the second as the formation rate of QPEs times the observation time Δt_{obs}. Therefore, in this work we estimate the QPE abundance per galaxy as

$$N_{QPE} = \Gamma_{TDE}\, \tau_{disk}\, \Gamma_{EMRI}\, \mu^{T,e,i}\, \bar{t}_{coal} \tag{7}$$

and the QPE formation rate per galaxy as

$$\Gamma_{QPE} = \Gamma_{TDE}\, \Gamma_{EMRI}\, \mu^{T,e,i}\, (\tau_{disk} + \bar{t}_{coal}) = N_{QPE} \left(\frac{1}{\tau_{disk}} + \frac{1}{\bar{t}_{coal}} \right). \tag{8}$$

We computed the cosmic volumetric abundance of QPEs by multiplying the per-galaxy abundance, $N_{QPE}(M_i, t)$ (Eq. (7)), by the local MBH mass function (that is, the number density of MBHs as a function of mass, see Fig. 3) and integrating over $M_\bullet$. We caution that this procedure implicitly assumes that TDE and EMRI rates are determined solely by the MBH mass and that all MBHs are surrounded by an NSC, which has been shown to dominate the production of TDEs (Polkas et al. 2024).

In practice, we simulated 0.5 dex equally log-spaced values of $M_\bullet$ (cf. Sect. 3.1.1) and computed the number density of QPEs n^i_{QPE} expected from MBHs in the i-th mass bin as

$$n^i_{QPE} = N_{QPE}(M_i, t) \int_{\Delta M_i} d \log_{10}(M_\bullet)\, \Phi(M_\bullet), \tag{9}$$

[3] See Section 2.

[4] We avoided introducing the time required for light to reach the observer, as it is a pure time shift. Moreover, for this computation we assumed that compatible EMRIs form a QPE immediately after they form. In fact, over these timescales the EMRI rate changes negligibly.

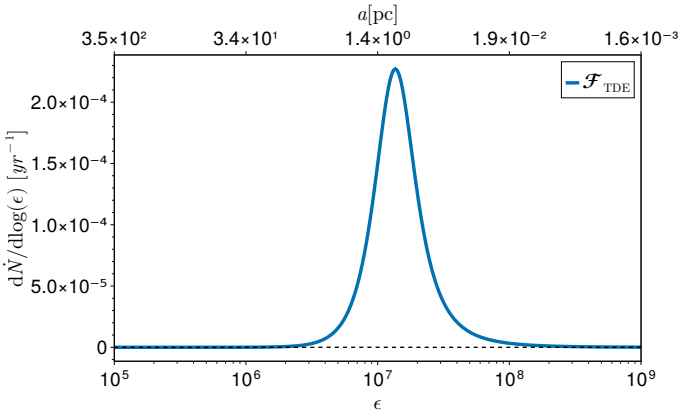


Fig. 4. Differential rate of TDEs, shown through the related function $d\dot{N}/d\log\epsilon = \epsilon\mathcal{F}_{\rm TDE}$ as a function of the absolute value of the orbital energy $\epsilon = -E$ for a star with $M_{\rm CO} = 1\,M_\odot$, $M_\bullet = 3\times10^6\,M_\odot$, at $t = 8\times10^6 yr$. The peak of $d\dot{N}/d\log\epsilon$ is located at $r_c(E) = 0.884$ pc

where ΔM_i is a 0.5 dex bin centered on the i-th value of the simulated MBH mass. We then estimated the cosmic QPE volumetric abundance, $\langle n_{QPE}\rangle$, by averaging $n^i_{\rm QPE}(t)$ over the total integration time, $t_{\rm end}$, for each bin and summing over all bins of $\log_{10} M_\bullet$

$$\left\langle n^i_{\rm QPE}\right\rangle = \frac{1}{t_{\rm end}}\int_0^{t_{\rm end}} dt\, n^i_{\rm QPE}(t) \tag{10}$$

$$\langle n_{\rm QPE}\rangle = \sum_i \left\langle n^i_{\rm QPE}\right\rangle . \tag{11}$$

3. Simulations of two-body relaxation and loss cone rates

For each system, we computed the TDE and EMRI rates and estimated the fraction of compact orbiters compatible with the disk-impact model for QPEs, by evolving the distribution function of stars and black holes in the Fokker-Planck formalism.

3.1. PhaseFlow runs

PhaseFlow is a publicly available code that simulates two-body relaxation in spherical isotropic stellar systems (Vasiliev 2017). It solves the ergodic Fokker-Planck equation (Cohn 1980) and includes a sink term to account for loss cone captures. The 1D approximation of relaxation in energy allows us to span a wide range of parameters over very long evolution times, whereas the full 2D problem in energy and angular momentum is significantly more computationally expensive.

3.1.1. Initial conditions

We considered systems with $\log_{10} M_\bullet/M_\odot = \{5, 5.5, 6, 6.5, 7, 7.5, 8\}$. For each MBH mass, we modeled the surrounding NSC with three stellar populations: one of stars and two of sBHs. The stellar component has a total mass of $20M_\bullet$ and consists of stars with a mass of $1\,M_\odot$. The sBH components consist of two populations with masses of $10\,M_\odot$ and $40\,M_\odot$, respectively. We chose their abundance such that the $10\,M_\odot$ accounted for a mass of $5/7\,M_\bullet$, while the $40\,M_\odot$ sBHs accounted for a mass of $2/7\,M_\bullet$[5]. As anticipated, the capture radius of stars is the tidal radius given by Eq. (1) over the range of $M_\bullet$ we considered. The capture radius for compact orbiters is the plunge radius given by Eq. (4) (see Subsection 2.1.2).

We set the size of the system so that the velocity dispersion σ of stars at the corresponding influence radius $r_h = G\,M_\bullet/\sigma^2$, lies on the $M_\bullet - \sigma$ relation (Ferrarese & Merritt 2000; Gebhardt et al. 2000). We computed σ according to the fit of Gültekin et al. (2009):

$$\sigma = 70\,{\rm km/s}\times\left(\frac{M_\bullet}{1.53\times10^6\,M_\odot}\right)^{1/4.24} . \tag{12}$$

Using the resulting influence radius, we initialized each of the three components (stars, lighter sBHs, and heavier sBHs) on a Dehnen profile with an inner slope 1.5 (Dehnen 1993; Tremaine et al. 1994):

$$\rho = \rho_0\left(\frac{r}{a}\right)^{-1.5}\left[1+\left(\frac{r}{a}\right)\right]^{-2.5} \tag{13}$$

where ρ_0 is the density normalization; $a = 4\,r_h$ is the scale radius that ensures the expected value of σ at the influence radius r_h.

The relaxation timescale of the system depends on its properties: in our case, the larger the total mass, the slower the relaxation. For cases with $M_\bullet \le 3\times10^6\,M_\odot$, we set a maximum timestep of 10^6 yr, and for the others a maximum timestep of 10^7 yr. In all cases, the total integration time was 10^{10} yr, as a proxy for the age of the Universe.

3.1.2. TDE rates

PhaseFlow tracks in time the number of stars entering the capture radius with a given energy $\mathcal{F}_{\rm TDE} = d\Gamma_{\rm TDE}/dE$ (see Fig. 4). From this quantity, the TDE rates at time t can be computed as:

$$\Gamma_{\rm TDE}(t) = \int_{-\infty}^{0} dE\,\mathcal{F}_{\rm TDE}(t,E). \tag{14}$$

and therefore

$$N_{\rm disks}(t) = \Gamma_{\rm TDE}(t)\,\tau_{\rm disk} . \tag{15}$$

3.1.3. EMRI rates

To distinguish EMRIs from direct plunges, we compared the angular momentum relaxation timescale and the GW timescale of loss cone orbits[6]. We recovered the angular momentum relaxation time of loss-cone orbits from PhaseFlow, which computes it internally, to calculate the disruption rate. Specifically, PhaseFlow gives the diffusion coefficient $\mathcal{D}$, so that the relaxation time of an orbit is given by Eq. (2). We computed the GW timescale according to Eq. (3). We then selected EMRIs as objects captured on orbits satisfying $t_{\rm GW} < t_{\rm rlx}$, as described in Sect. 2.1.2.

Using the loss cone flux of a component $\mathcal{F}_{\rm CO} = d\Gamma_{\rm CO}/dE$ (see Fig. 5), we computed the rate of EMRI formation of that component as (see Fig. 6)

$$\Gamma_{\rm EMRI}(t) = \int_{-\infty}^{E_{\rm GW}} dE\,\mathcal{F}_{\rm CO}(t,E) \tag{16}$$

[5] The proportions in total mass among the components match those obtained from the Kroupa initial mass function (see Spera et al. 2016).
[6] For a semi-analytical approach to the 2D Fokker-Planck equation, see Kaur et al. (2025).

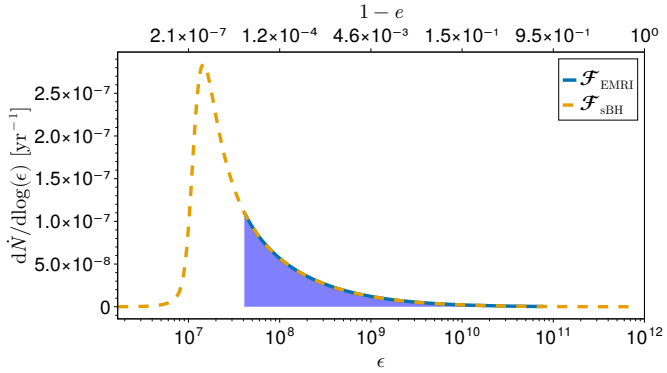


Fig. 5. Differential rate of EMRIs $\mathcal{F}_{\rm EMRI}$ and direct plunges $\mathcal{F}_{\rm sBH}$ as functions of the energy ϵ and the eccentricity of the loss-cone orbit e. We consider sBHs of $M_{\rm CO} = 40\,M_\odot$ in a system with $M_\bullet = 3\times10^6\,M_\odot$ that has undergone relaxation for 1 Gyr. Our estimate of the EMRI rate is given by the light-blue shaded area. The eccentricity at the peak of the differential rate is $1 - e = 3.35\times10^{-7}$.

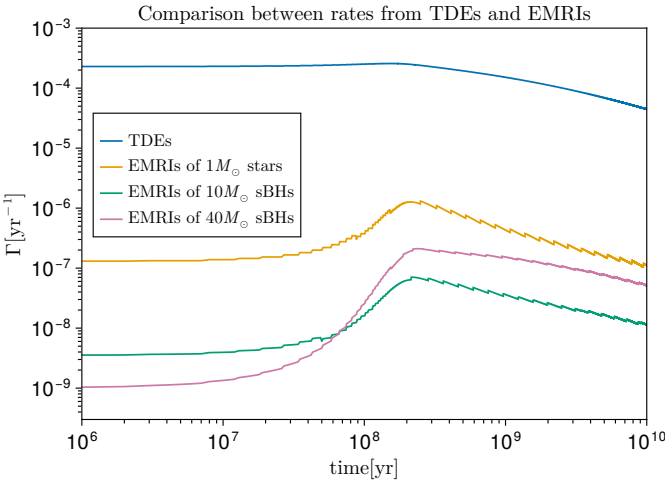


Fig. 6. Time-dependent EMRI rates for $1\,M_\odot$ stars (orange), $10\,M_\odot$ sBHs (green), and $40\,M_\odot$ sBHs (pink), together with TDE rates (blue), for $M_\bullet = 3\times10^6\,M_\odot$.

where $E_{\rm GW}$ is the energy at which the curve $t_{\rm GW} = t_{\rm rlx}$ crosses the loss cone. We computed the total number of EMRIs from that component by integrating over the $t_{\rm rlx} = t_{\rm GW}$ line as

$$N^{tot}_{\rm EMRI} = \int {\rm d}E\, \mathcal{F}_{\rm CO}(t, E)\, t_{\rm coal}(E) \tag{17}$$

where $t_{\rm coal}(E)$ is the time-to-coalesce starting from the $t_{\rm rlx} = t_{\rm GW}$ curve with energy E.

4. Abundance and formation rate of QPEs

As introduced in Sect. 2.2, we computed the number of disks, $N_{\rm disk}$, around the MBH by multiplying the instantaneous $\Gamma_{\rm TDE}(t)$ for $\tau_{\rm disk}$. In contrast, the number of compact orbiters depends on the details of the model and crucially on its constraints on inclination and eccentricity at the QPE semimajor axis. Typical EMRI semimajor axes range from $\sim10^{-5}$–10^{-1}pc, with periods much longer than those of observed QPEs. Assuming the Keplerian estimate[7],

$$a_{\rm QPE} \simeq \sqrt[3]{GM_\bullet\left(\frac{T_{\rm QPE}}{\pi}\right)^2} \tag{18}$$

we considered, for reference, [8]

$$a(48\,{\rm h}) = 2.38\times10^{-7}\,{\rm pc}\times\left(\frac{M_\bullet}{M_\odot}\right)^{1/3}, \tag{19}$$

$$a(20\,{\rm h}) = 1.34\times10^{-7}\,{\rm pc}\times\left(\frac{M_\bullet}{M_\odot}\right)^{1/3}, \tag{20}$$

$$a(9\,{\rm h}) = 7.5\times10^{-8}\,{\rm pc}\times\left(\frac{M_\bullet}{M_\odot}\right)^{1/3}, \tag{21}$$

$$a(2\,{\rm h}) = 2.9\times10^{-8}\,{\rm pc}\times\left(\frac{M_\bullet}{M_\odot}\right)^{1/3}. \tag{22}$$

4.1. Constraints on eccentricity and inclination

Once we fixed the maximum a of observable QPEs $a^{\rm max}_{\rm QPE}$ and the maximum e compatible with the model $e^{\rm max}_{\rm QPE}$, we evolved the EMRIs formed on the $t_{\rm rlx} = t_{\rm GW}$ line until their a and e were both within the constraints (cf. the dashed black area in Fig. 2). While $a^{\rm max}_{\rm QPE}$ can be constrained observationally from the typical recurrence timescales (through the period–semimajor-axis mapping), the same is not true for $e^{\rm max}_{\rm QPE}$. The relevant eccentricity threshold depends on the (still uncertain) physical mechanism responsible for QPE emission, and therefore we treated $e^{\rm max}_{\rm QPE}$ as a model parameter.

We used the following strategy to compute the number of active QPEs from a snapshot of PHASEFLOW. For each energy bin along the $t_{\rm rlx} = t_{\rm GW}$ line, we took its center as the initial point of an EMRI trajectory (see Fig. 2). From the 2.5 post-Newtonian, orbit-averaged trajectory (Peters 1964), we determined the eccentricity e_1 such that $a(e_1) = a^{\rm max}_{\rm QPE}$, with

$$a(e) = c_0\,\frac{e^{12/19}}{1-e^2}\left[1+\frac{121}{304}e^2\right]^{870/2299}. \tag{23}$$

where c_0 is determined by the initial conditions for a and e. If $e_1 < e^{\rm max}_{\rm QPE}$, the trajectory is compatible with QPE orbiters from $(e_1, a^{\rm max}_{\rm QPE})$ to coalescence. If $e_1 > e^{\rm max}_{\rm QPE}$, we further evolved the trajectory up to $a_1 = a(e^{\rm max}_{\rm QPE})$; this trajectory is then compatible with QPE orbiters from $(e^{\rm max}_{\rm QPE}, a_1)$ until coalescence.

Fig. 2 shows detailed examples of the possible evolution in the $(1-e, a)$ phase space for two sBHs, as well as the selected $(1-e, a)$ parameters of QPEs given $(1-e^{\rm max}_{\rm QPE}, a^{\rm max}_{\rm QPE})$.

We treated the process of two-body scattering under the assumption of spherical symmetry. In a spherically symmetric potential around a non-spinning MBH, we expect the orbital angular-momentum directions of bound sBHs and stars to be isotropically distributed, i.e., with random orbital inclination i. This assumption may break down if MBH spin (Kerr geometry) and relativistic precession introduce a preference for prograde or low-inclination orbits, potentially modifying EMRI rates and

[7] We assume that the $T_{\rm QPE}$ is half the orbital period, as the sBH typically pierces the accretion disk twice during each radial period.

[8] We chose values corresponding to the recurrence period of AT2022upj (48 h) (Chakraborty et al. 2025), eRO-QPE3 (20 h) (Arcodia et al. 2024), GSN069 (9 h) (Miniutti et al. 2019), and eRO-QPE2 (2 h) (Arcodia et al. 2021).

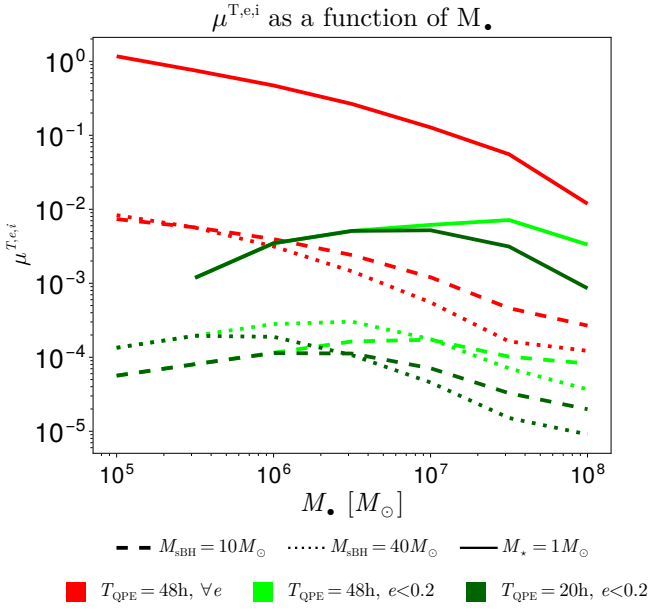


Fig. 7. QPE selection factor $\mu^{T,e,i} = N_{CO}/N^{tot}_{\rm EMRI}$ as a function of $M_\bullet$, for different values of the maximum period $T_{\rm QPE}$, and the maximum eccentricity $e^{\rm max}_{\rm QPE}$ compatible with QPEs.

the inclination distribution. Accordingly, we set the direction of angular momentum to be uniformly distributed on the sphere at the beginning of the GW-dominated phase. The probability that the relative i between the TDE disk and the EMRI orbit is smaller than $i^{\rm max}_{\rm QPE}$ is:

$$P(0 < i < i^{\rm max}_{\rm QPE}) = \frac{1}{2}\int_0^{i^{\rm max}_{\rm QPE}} d\theta \sin\theta \tag{24}$$

and for sBHs we choose a typical value $i^{\rm max}_{\rm QPE} = 20°$, giving $P(i < i^{\rm max}_{\rm QPE}) = 0.03$. We set no constraints on the inclination of stellar EMRIs.

4.2. Coalescence time and $N_{\rm CO}$

Given that EMRIs formed with energy E are compatible with QPEs only from $(e_1, a^{\rm max}_{\rm QPE})$ or $(e^{\rm max}_{\rm QPE}, a_1)$, we computed $N_{\rm CO}$ by evaluating the coalescence time from that location. We estimate it as (Peters 1964)

$$t^{\rm QPE}_{coal}(E) = \frac{12}{19}\frac{c_0^4}{\beta} \times \int_{e_{\rm fin}}^{e_{\rm QPE}} \frac{de\, e^{29/19}[1 + (121/304)e^2]^{1181/2299}}{(1-e^2)^{3/2}} \tag{25}$$

where c_0 is the quantity appearing in Eq. (23), while $e_{\rm QPE} = e_1$ or $e^{\rm max}_{\rm QPE}$, and $e_{\rm fin}$ is the eccentricity at merger or disruption. Consequently, $r_{\rm cap} = a(e_{\rm fin})(1 - e_{\rm fin})$ for sBHs, while for stars it is the solution of $a(e_{\rm fin})(1 - e_{\rm fin}) = r_t$ using Eq. (23).

We combined these ingredients to compute the expected number of orbiters compatible with the QPE model:

$$N_{\rm CO}(t) = \int {\rm d}E\, \mathcal{F}_{\rm EMRI}(t, E)\, t^{\rm QPE}_{\rm coal}(E)\,. \tag{26}$$

Then, using Eqs. (26) and (15), we computed the number of active QPEs as $N_{\rm QPE} = N_{\rm disks}\, N_{\rm CO}$.

5. Results

This section summarizes the results of our analysis on the number of QPEs in the NSCs considered and their inferred cosmic abundance. To estimate these quantities, we first evaluated the average QPE selection factor $\mu^{T,e,i}$, namely the fraction of EMRIs that satisfy the conditions required to be compatible with QPEs over 10 Gyr of simulation. The corresponding values are reported in Table A.1 of Appendix A. We note that it is defined in terms of three parameters: the maximum inclination, $i^{\rm max}_{\rm QPE}$, the maximum eccentricity, $e^{\rm max}_{\rm QPE}$, and the maximum orbital period, $T_{\rm QPE}$. Although the disk-impact model does not impose direct constraints on the eccentricity of stellar orbiters, the impact of $e^{\rm max}_{\rm QPE}$ is non-trivial, so we include it for completeness. We set $i^{\rm max}_{\rm QPE} = 20°$ for sBHs and impose no constraints on i for stars. The scalings of $\dot{a}$ and $\dot{e}$ directly impact the trend of $\mu^{T,e,i}$ due to GW emission. At fixed constraints on e and T, the fraction of COs compatible with QPEs decreases with increasing $M_\bullet$ at the higher-mass end, because $T_{\rm QPE}$ selects an increasingly smaller fraction of EMRIs. At the low-mass end, GW-driven circularization can instead reduce $\mu^{T,e,i}$, especially for sBHs (see Fig. 7). The number of objects with semimajor axes smaller than a behaves like $t_{\rm GW}$ (e.g., Amaro-Seoane et al. 2017), setting the scaling of $\mu^{T,e,i}$ for $e^{\rm max}_{\rm QPE} = 1$. As $t_{\rm GW} \sim a^{1/2} \sim T^{1/3}$ for very eccentric orbits and $t_{\rm GW} \sim a^4 \sim T^{8/3}$ for nearly circular orbits, the scalings we find are bounded by these two extremes. Due to the mixed eccentricity distribution, $\mu^{T,e,i}$ is almost linear with $T_{\rm QPE}$ at $M_\bullet = 10^5\, M_\odot$, while it becomes steeper for larger $M_\bullet$ (see Fig. 8). In general, most EMRIs are found at moderate eccentricities, so the impact of the eccentricity cut is evident for both sBHs and stars: larger $e^{\rm QPE}_{\rm max}$ gives larger $\mu^{T,e,i}$, although the magnitude of the change depends on the mass of the stellar object and the NSC. The selection factor $\mu^{T,e,i}$ is generally comparable between the two species of sBHs, but is typically larger for stars because there is no inclination constraint and they are lighter. In fact, the GW-dominated region for stars is smaller, and a larger fraction corresponds to periods compatible with QPEs. However, for large $M_\bullet$, the period at r_t is so long that $\mu^{T,e,i} = 0$ for the shortest values of $T_{\rm QPE}$. For SMBH masses of $3 \times 10^7\, M_\odot$ and $10^8\, M_\odot$, the same occurs when the period at $r_{\rm cap}$ is longer than $T_{\rm QPE}$ (see Table A.1 of Appendix A).

We then used the selection factor $\mu^{T,e,i}$ to estimate the number of active QPEs, $N_{\rm QPE}$, in each NSC. Figs. 9 and 10 show the evolution of $N_{\rm QPE}$ for two representative systems. Since $N_{\rm QPE}$ can be related to the formation rate through Eq. (8), assuming $\tau_{\rm disk} \ll \bar{t}_{\rm coal}$, we have $\Gamma_{\rm QPE} = N_{\rm QPE}/\tau_{\rm disk}$, and the two quantities therefore follow the same trend. At $t \gtrsim 1$ Gyr, $N_{\rm QPE}$ starts to decline, following the long-term evolution of loss cone event rates. Table A.2 of Appendix A lists the time-averaged value $\langle N_{\rm QPE}\rangle$ over 10 Gyr for all of the NSCs we considered. Since $N^{\rm tot}_{\rm EMRI}$ depends weakly on the mass of the orbiter at fixed $M_\bullet$, $\langle N_{\rm QPE}\rangle$ follows the same qualitative trends as $\mu^{T,e,i}$. Similarly, the scaling of the loss cone rates with $M_\bullet$ weakly affects that of $\mu^{T,e,i}$.

Finally, we combined our results with the MBH mass function to compute the cosmic QPE abundance $\langle n_{\rm QPE}\rangle$, as described in Subsection 2.2. Fig. 11 presents $\langle n_{\rm QPE}\rangle$ for $T_{\rm QPE} = \{2, 9, 20, 48\}$ h and $e^{\rm max}_{\rm QPE} = \{0.05, 0.2, 1\}$ [9]. For $T_{\rm QPE} \gtrsim 9$ h, rates can vary by $2-3$ orders of magnitude depending on the adopted eccentricity constraints, and by less than an order of magnitude

[9] Physically, the maximum possible eccentricity is set by the minimum pericenter $r_{\rm cap}$ or r_t.

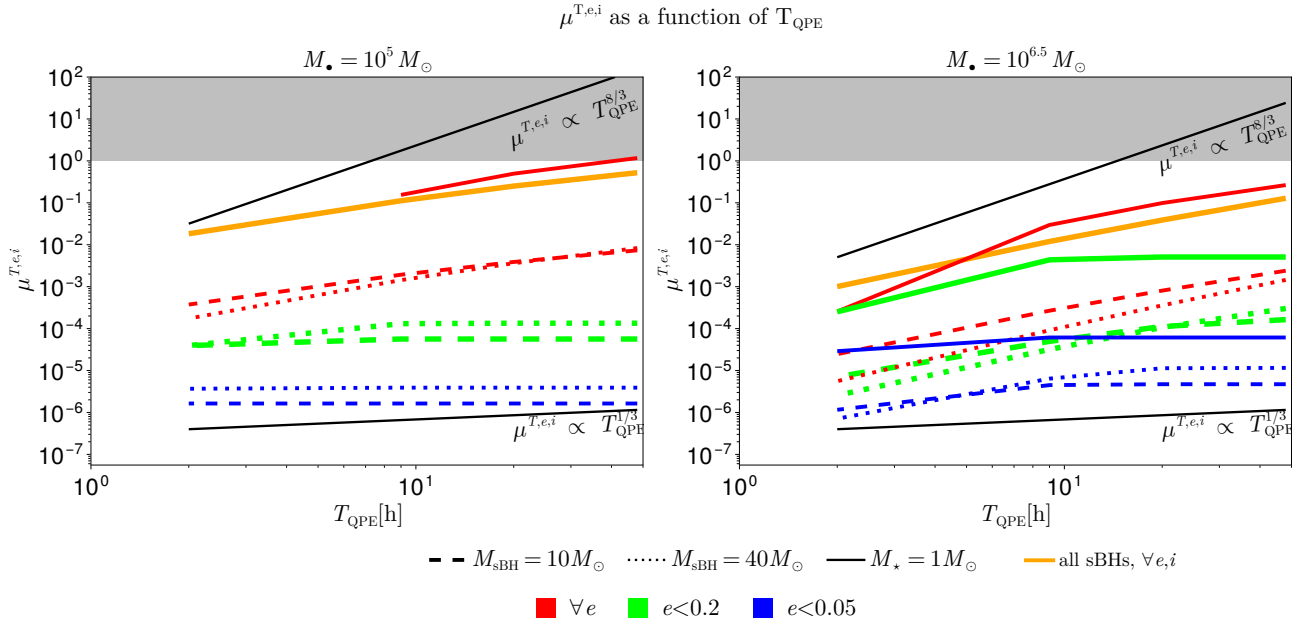


Fig. 8. QPE selection factor $\mu^{T,e,i} = N_{CO}/N^{tot}_{\mathrm{EMRI}}$ for $M_\bullet = 10^5\,M_\odot$ (left) and $M_\bullet = 3\times10^6\,M_\odot$ (right), for different values of the maximum period T_{QPE} and the maximum eccentricity $e^{\mathrm{max}}_{\mathrm{QPE}}$ compatible with QPEs. The gray region marks parameter values for which μ would exceed unity; these are unphysical because μ is defined as a fraction of all EMRIs (hence $0 \le \mu \le 1$).

depending on the period constraints. Overall, stellar QPEs are $\sim 10^3$ more numerous than sBH QPEs at fixed constraints.

Arcodia et al. (2024) estimate a cosmic QPE abundance of $(1.7\times10^{-7} - 5\times10^{-6})$ Mpc^{-3}, which is compatible with our estimates for QPEs in the disk-impact model from stellar EMRIs. When we remove eccentricity and inclination constraints, sBH QPEs are compatible with the lower end of these estimates, as discussed in the next section.

6. Discussion

6.1. EMRI formation channels

We now discuss the assumptions and limitations of our results, beginning with the EMRI formation channels considered in our model. We focus on the classical EMRI formation channel, but various alternative dynamical channels have been proposed. Among these, some might have cosmological rates comparable to or higher than spherical two-body relaxation, especially when restricting to small eccentricities and sBHs. For example, a member of a stellar binary might be deposited as a result of a three-body encounter with the central MBH (Binary deposition Miller et al. 2005). Such a channel might favor small eccentricities with comparable rates (Raveh & Perets 2021). If the central MBH is surrounded by a disk, it can capture compact objects through inclination damping and further reduce their orbital eccentricity as they migrate toward the MBH (e.g., Syer et al. 1991; Šubr & Karas 1999; Karas & Šubr 2001; Levin 2007; Kocsis et al. 2011). This channel seems very promising for producing EMRIs (see Pan & Yang 2021) with small eccentricities (Sun et al. 2026). Alternatively, a star or an sBH might form in the disk (e.g., Artymowicz et al. 1993; Levin 2003; Goodman & Tan 2004), or multiple mergers might increase the size of sBHs. Since EMRI formation rates in these scenarios are subject to very large uncertainties, we do not attempt to compute the corresponding expected QPE rates; however, the current formalism can be readily applied to any EMRI formation channel.

6.2. Dependence of the cosmic volumetric abundance on the TDE disk lifetime

Throughout this work, we adopt a fiducial TDE disk lifetime of $\tau_{\mathrm{disk}} = 10\,\mathrm{yr}$, motivated by viscous disk-evolution models for TDE debris disks (e.g., Cannizzo et al. 1990; Montesinos Armijo & de Freitas Pacheco 2011; Piro & Mockler 2025). The physical value of τ_{disk} is uncertain and may depend on several parameters, including the mass of the disrupted star, the MBH mass, the accretion efficiency, the viscosity parameter, the disk aspect ratio, and the circularization radius. Therefore, the assumption of a single disk lifetime for all MBH masses should be regarded as an effective choice rather than as a universal property of TDE disks. The impact of this assumption on our results follows directly from the definition of the active QPE abundance N_{QPE}, which is linearly proportional to τ_{disk} (see Eq. (7)). This linear dependence propagates directly to the cosmic volumetric abundance, since we obtain n^i_{QPE} by multiplying $N_{\mathrm{QPE}}(M_i, t)$ by the MBH mass function in each mass bin (Eq. (9)), and $\langle n_{\mathrm{QPE}}\rangle$ is obtained by time-averaging and summing over the MBH mass bins (Eqs. (10)–(11)). Consequently, if we adopt a different but mass-independent value of τ_{disk}, all volumetric abundances shown in Fig. 11 can be rescaled by the same multiplicative factor. If instead τ_{disk} depends on $M_\bullet$, the rescaling must be performed separately in each MBH mass bin, potentially altering the relative contribution of the different bins to the total abundance. Such a rescaling is sufficient only when the underlying stellar and dynamical model is kept fixed. This alters the range of MBH masses for which disruption occurs, as well as the resulting disk properties, potentially affecting the TDE rate, disk lifetime, and QPE-selection factor. Therefore, varying only τ_{disk} produces a simple multiplicative rescaling, whereas changing the stellar model may require the TDE and QPE-selection calculations to be recomputed consistently and can modify both the normalization and the MBH-mass dependence of the predicted QPE abundance. Our fiducial comparison with the observational abundance estimated by Arcodia et al. (2024)

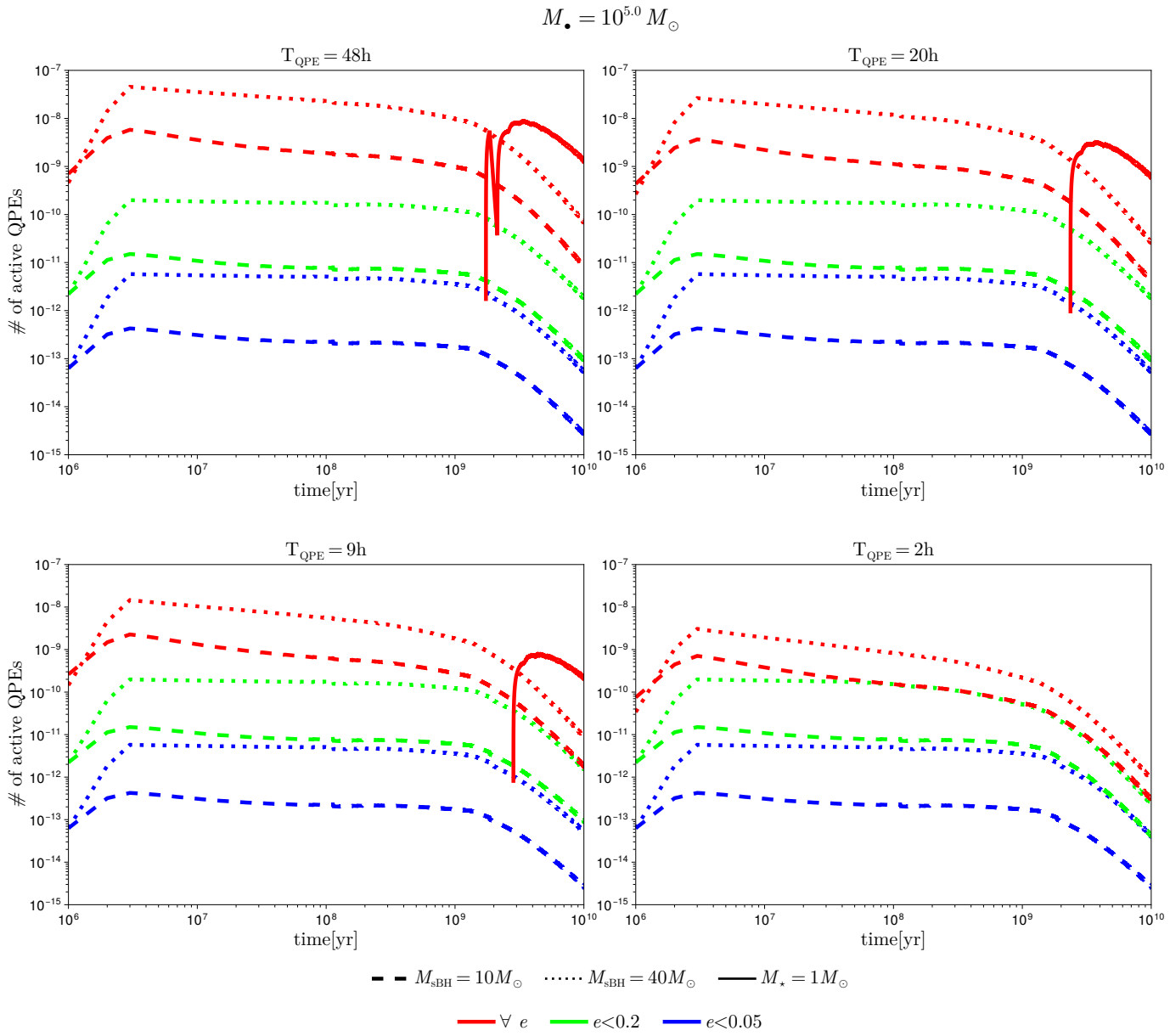


Fig. 9. Number of active QPEs from $10M_\odot$ sBHs (dashed line), $40\,M_\odot$ (dotted line) sBHs, and $1M_\odot$ stars (solid line) around an MBH of $10^5 M_\odot$. Different colors indicate different limiting eccentricities, as marked in the figure. The four panels show different values of T_{QPE}: T_{QPE} = 48 h (top left), 20 h (top right), 9 h (bottom left), and 2 h (bottom right).

is consistent because both analyses adopt a reference timescale of 10yr. Although the two timescales have different physical meanings, our disk lifetime coincides with the fiducial QPE lifetime, τ_{life} = 10yr, adopted by Arcodia et al. (2024) when converting their observed abundance into a formation rate. However, their abundance estimate is independent of τ_{life}, whereas our predicted abundance scales linearly with τ_{disk}. Significantly different values of τ_{disk} would therefore shift our predictions and modify the comparison.

6.3. Dynamics in the NSC

As explained in Sect. 2, the effects of GW emission are not included in 1D Fokker-Planck models as PHASEFLOW, primarily because of the significant impact of eccentricity. We neglected the spin of the primary MBH, which might increase the number of EMRIs and affect the inclination distribution (e.g., Zhang & Amaro Seoane 2026; Sun et al. 2026). Deviations from spherical symmetry might increase the loss cone rates, most importantly the TDE rate, although the impact might be minor for the small MBHs we considered (Vasiliev & Merritt 2013). Similarly, a steep gaseous profile might affect the evolution of objects through significant dynamical friction (Rozner & Ramirez-Ruiz 2025).

Currently, loss cone theory neglects partial tidal disruptions and Roche lobe overflow, only accounting for the possibility of complete tidal disruption (Cohn & Kulsrud 1978; Merritt 2013; Broggi 2025). The TDE rate might be marginally affected at small $M_\bullet$ (e.g., Bortolas et al. 2023; Broggi et al. 2024). However, because EMRIs require repeated passages at small peri-

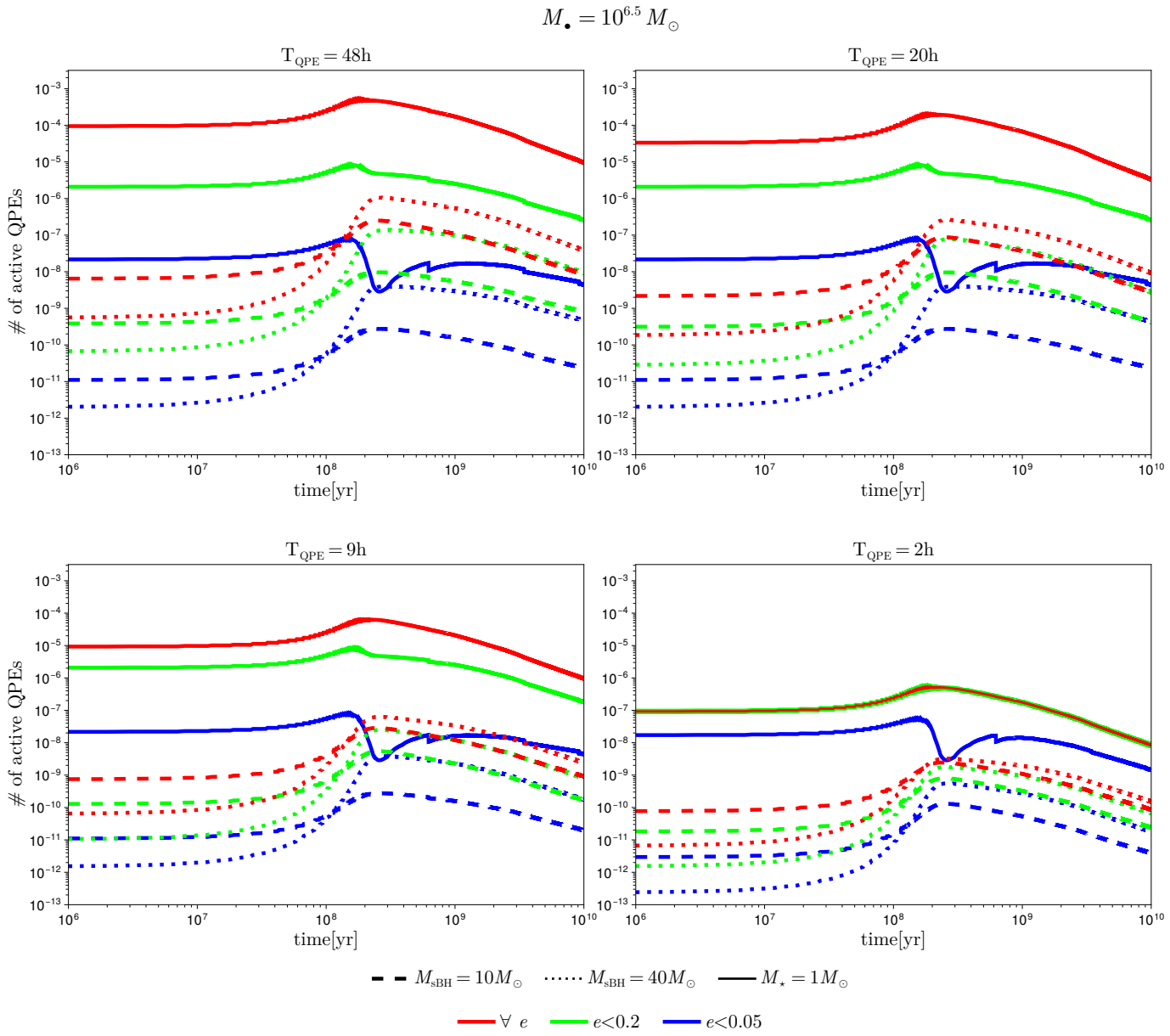


Fig. 10. Same as Fig. 9 but for a central MBH of $3 \times 10^6 M_\odot$

center, these effects might significantly affect the rate of stellar EMRIs and, consequently, the related QPE abundance.

6.4. Galactic population

We assumed that every MBH is surrounded by an NSC whose properties are fixed by its mass. Naturally, not all MBHs have an NSC. Moreover, the properties of NSCs vary systematically with host galaxy mass and morphology (Neumayer et al. 2020), suggesting that the initial phase of the relaxation process and the total available mass budget in our simple NSC model might be inadequate. At later stages, relaxation dictates the stellar profile, possibly reducing the uncertainty when considering the cosmic population. Finally, we represented the stellar population using only three discrete mass components. This approximation captures the main effects of mass segregation, but it necessarily simplifies the underlying continuous stellar mass spectrum. Different stellar masses segregate on different timescales and contribute differently to relaxation. In particular, massive remnants tend to concentrate more strongly toward the MBH and can enhance the relaxation experienced by lighter objects, while low-mass stars remain less centrally concentrated. A broader mass spectrum could therefore modify both the relative abundance of the different populations near the MBH and the time-dependent TDE and EMRI rates (Bortolas 2022). Moreover, the mass of the inspiraling object directly affects its GW-driven evolution and coalescence timescale. Therefore, if timing models provide observational constraints on the masses of stellar EMRIs, a more detailed treatment of the population mass spectrum would be required to model both their dynamical distribution and GW evolution consistently. Our three-component treatment should therefore be regarded as an effective description rather than a complete representation of the mass dependence of the population.

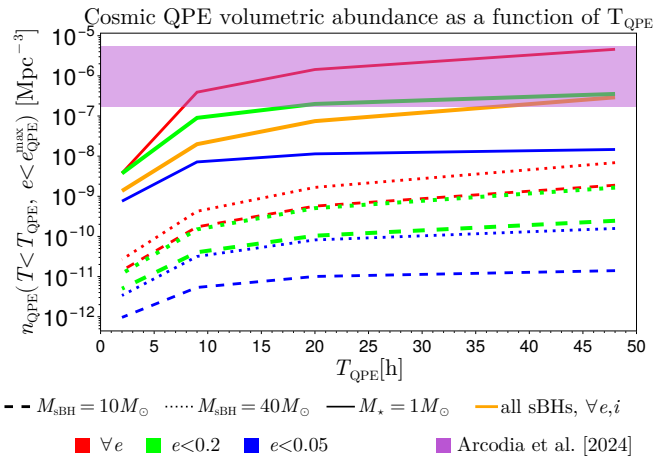


Fig. 11. Cosmic volumetric abundance assuming limiting eccentricities of 0.05, 0.2, and 1.0 for $10M_\odot$ sBHs (dashed line) and $40M_\odot$ sBHs (dotted line). The cosmic volumetric abundance of stars (solid line) is portrayed at e = 0.05, 0.2, 1-r_t/a_{QPE}. The orange solid line represents the sum of n_{QPE} for both sBHs without accounting for the constraints on e and i. The violet band represents the QPE volumetric abundance found by Arcodia et al. (2024).

6.5. Observability of QPEs

We did not include observability constraints on disk and EMRI systems. However, emission mechanisms with a preferential axis or the properties of the TDE disk might reduce the number of observable systems. In fact, electromagnetic emission in the disk-impact model is not fully understood. The bubble generated as the object crosses the disk cools until it becomes optically thin; at that stage, its temperature settles at the inferred temperature T_{obs}, which is set by the cooling process. These open points directly affect our rates through orbital constraints. For example, very eccentric EMRIs from sBHs might reach pericenters so small that the disk density is considerable; despite the small Bondi radius, the passage might strip as much mass as in the circular case, producing a comparably luminous flare and thus relaxing eccentricity constraints.

6.6. Constraints from timing models

The first results from the fitting of the timing of QPEs with dynamical models (see e.g., Zhou et al. 2024) indicate a preference for small eccentricities, without assumptions about the type of orbiter. While this might be caused by the size of the Bondi radius for sBHs, stellar QPEs from standard two-body relaxation should favor large eccentricities. Restricting the maximum eccentricity affects the expected number density of QPEs by orders of magnitude, possibly pushing it outside the currently inferred range.

7. Conclusions

We built a framework to compute the number of expected QPEs produced by two-body relaxation in the disk-impact model. We assumed a Schwarzschild MBH and a spherically symmetric potential.

We linked the QPE volumetric abundance to the formation rates of EMRIs and TDEs. We modeled these rates by simulating the relaxation of NSCs around MBHs with masses $M_\bullet = 10^5 - 10^8\ M_\odot$ using the Fokker-Planck integration code PHASEFLOW (Vasiliev 2017).

We modeled each NSC with three mass components: main sequence stars with masses $1M_\odot$ and two families of sBHs with masses of $10M_\odot$ and $40M_\odot$. We evolved the systems for 10 Gyr and tracked the evolution of the TDE and EMRI rates. Finally, we selected EMRI events that satisfied the constraints arising from the emission model: a maximum orbital period T_{QPE} and, for sBHs, a maximum eccentricity $e_{QPE}^{max} \simeq 0.2$ and the maximum inclination $0 < i < i_{QPE}^{max} \simeq 20°$. We assumed that all MBHs are surrounded by an NSC and combined our results with the black hole mass function to estimate the QPE abundance in the Universe.

We find that the QPE volumetric abundance (or number density) can vary from 10^{-12} Mpc^{-3} to 10^{-6} Mpc^{-3}, depending on the imposed constraints (see Fig. 11). The QPEs powered by impacting stars can be as frequent as suggested by the first observational estimates (Arcodia et al. 2024). Conversely, the constraints on the orbital properties of sBHs significantly reduce the number of observable QPEs, which are $\sim 10^3$ times less numerous than stellar QPEs and generally below observational estimates.

When we remove inclination and eccentricity constraints, the total number of QPEs from sBHs is compatible with the lower end of the observational predictions for T_{QPE} = 48 h, whereas the number of QPEs from stars is compatible with observational estimates for $T_{QPE} > 9$ h. In general, two-body relaxation induces a preference for eccentric sources, in contrast with the picture emerging from fits to QPE timing and, for sBH-driven QPEs, from constraints on the Bondi radius. Restricting the population to low-eccentricity sources significantly reduces the rate, possibly to values incompatible with observational estimates both for stars and sBHs. In our model, restricting sBH-driven QPEs to low-inclination systems reduces their predicted rate by a factor of ∼30. By contrast, Liu et al. (2026) adopt the Hill radius as the relevant impact scale for sBHs, which is independent of the orbital inclination. This assumption therefore allows a broader range of orbital configurations and increases the predicted number of sBH-driven QPEs.

By including other formation channels for EMRIs, a more detailed dynamical model, and more refined galactic models, it may be possible to probe, constrain, and rule out dynamical models of QPEs. Shedding light on their nature and understanding their possible connection to EMRIs may establish them as electromagnetic counterparts of future Laser Interferometer Space Antenna (LISA) sources, opening new avenues in multi-messenger astronomy.

Acknowledgements. AS acknowledges financial support provided under the European Union's H2020 ERC Advanced Grant "PINGU" (Grant Agreement: 101142079). MB acknowledges support from the Italian Ministry for Universities and Research (MUR) program "Dipartimenti di Eccellenza 2023–2027", within the framework of the activities of the Centro Bicocca di Cosmologia Quantitativa (BiCoQ). We thank A. Franchini for useful discussions and valuable comments. C.M.A. and L.B. thank D. Mancieri for helpful suggestions, especially on the figures and their graphical presentation.

References

Amaro-Seoane, P., Audley, H., Babak, S., et al. 2017, Laser Interferometer Space Antenna, Tech. rep., LISA Consortium
Arcodia, R., Merloni, A., Nandra, K., et al. 2021, Nature, 592, 704
Arcodia, R., Liu, Z., Merloni, A., et al. 2024, A&A, 684, A64
Artymowicz, P., Lin, D. N. C., & Wampler, E. J. 1993, ApJ, 409, 592
Bar-Or, B., & Alexander, T. 2016, ApJ, 820, 129

Bondi, H. 1952, MNRAS, 112, 195
Bonnerot, C., & Lu, W. 2020, MNRAS, 495, 1374
Bortolas, E. 2022, MNRAS, 511, 2885
Bortolas, E., Ryu, T., Broggi, L., & Sesana, A. 2023, MNRAS, 524, 3026
Broggi, L. 2025, Phys. Rev. Lett., 135, 231201
Broggi, L., Stone, N. C., Ryu, T., et al. 2024, Open J. Astrophys., 7, 48
Cannizzo, J. K., Lee, H. M., & Goodman, J. 1990, ApJ, 351, 38
Chakraborty, J., Kara, E., Masterson, M., et al. 2021, ApJ, 921, L40
Chakraborty, J., Arcodia, R., Kara, E., et al. 2024, ApJ, 965, 12
Chakraborty, J., Kara, E., Arcodia, R., et al. 2025, ApJ, 983, L39
Cohn, H. 1979, ApJ, 234, 1036
Cohn, H. 1980, ApJ, 242, 765
Cohn, H., & Kulsrud, R. M. 1978, ApJ, 226, 1087
Curd, B. 2021, MNRAS, 507, 3207
Dai, L. J., Fuerst, S. V., & Blandford, R. 2010, MNRAS, 402, 1614
Dehnen, W. 1993, MNRAS, 265, 250
Ferrarese, L., & Merritt, D. 2000, ApJ, 539, L9
Franchini, A., Bonetti, M., Lupi, A., et al. 2023, A&A, 675, A100
Gebhardt, K., Bender, R., Bower, G., et al. 2000, ApJ, 539, L13
Giustini, M., Miniutti, G., & Saxton, R. D. 2020, A&A, 636, L2
Goodman, J., & Tan, J. C. 2004, ApJ, 608, 108
Gültekin, K., Richstone, D. O., Gebhardt, K., et al. 2009, ApJ, 698, 198
Guolo, M., Pasham, D. R., Zajaček, M., et al. 2024, Nat. Astron., 8, 347
Hernández-García, L., Chakraborty, J., Sánchez-Sáez, P., et al. 2025, Nat. Astron., 9, 895
Hills, J. G. 1975, Nature, 254, 295
Hopman, C., & Alexander, T. 2005, ApJ, 629, 362
Izquierdo-Villalba, D., Sesana, A., Colpi, M., et al. 2024, A&A, 686, A183
Karas, V., & Šubr, L. 2001, A&A, 376, 686
Kaur, K., Stone, N. C., & Gilbaum, S. 2023, MNRAS, 524, 1269
Kaur, K., Rom, B., & Sari, R. 2025, ApJ, 980, 150
Kocsis, B., Yunes, N., & Loeb, A. 2011, Phys. Rev. D, 84, 024032
Levin, Y. 2003, ArXiv e-prints [arXiv:astro-ph/0307084]
Levin, Y. 2007, MNRAS, 374, 515
Linial, I., & Metzger, B. D. 2023, ApJ, 957, 34
Liu, K., Liu, S.-F., Pan, Z., et al. 2026, ApJ, 1006, L50
Lodato, G., & Rossi, E. M. 2010, MNRAS, 410, 359
Lodato, G., Franchini, A., Bonnerot, C., & Rossi, E. M. 2015, J. High Energy Astrophys., 7, 158
Mancieri, D., Broggi, L., Bonetti, M., & Sesana, A. 2025, A&A, 694, A272
Mancieri, D., Broggi, L., Vinciguerra, M., Sesana, A., & Bonetti, M. 2026, Phys. Rev. D, 113, 043062
Merritt, D. 2013, CQG, 30, 244005
Miller, M. C., Freitag, M., Hamilton, D. P., & Lauburg, V. M. 2005, ApJ, 631, L117
Miniutti, G., Saxton, R. D., Giustini, M., et al. 2019, Nature, 573, 381
Miniutti, G., Giustini, M., Arcodia, R., et al. 2023, A&A, 670, A93
Montesinos Armijo, M., & de Freitas Pacheco, J. A. 2011, ApJ, 736, 126
Mummery, A., & Balbus, S. A. 2020, MNRAS, 492, 5655
Neumayer, N., Seth, A., & Böker, T. 2020, A&ARv, 28, 4
Nicholl, M., Pasham, D. R., Mummery, A., et al. 2024, Nature, 634, 804
Pan, Z., & Yang, H. 2021, Phys. Rev. D, 103, 103018
Pan, X., Li, S.-L., Cao, X., Miniutti, G., & Gu, M. 2022, ApJ, 928, L18
Peters, P. C. 1964, Phys. Rev., 136, 1224
Phinney, E. S. 1989, IAU Symp., 136, 543
Piro, A. L., & Mockler, B. 2025, ApJ, 985, 77
Polkas, M., Bonoli, S., Bortolas, E., et al. 2024, A&A, 689, A204
Quintin, E., Webb, N. A., Guillot, S., et al. 2023, A&A, 675, A152
Qunbar, I., & Stone, N. C. 2024, Phys. Rev. Lett., 133, 141401
Raveh, Y., & Perets, H. B. 2021, MNRAS, 501, 5012
Rees, M. J. 1988, Nature, 333, 523
Rozner, M., & Ramirez-Ruiz, E. 2025, ApJ, 988, L21
Shen, R.-F., & Matzner, C. D. 2014, ApJ, 784, 87
Śniegowska, M., Grzędzielski, M., Czerny, B., & Janiuk, A. 2023, A&A, 672, A19
Spera, M., Giacobbo, N., & Mapelli, M. 2016, Mem. Soc. Astron. It., 87, 575
Spitzer, L. 1987, Dynamical evolution of globular clusters
Stone, N. C., Vasiliev, E., Kesden, M., et al. 2020, Space Sci. Rev., 216, 35
Šubr, L., & Karas, V. 1999, A&A, 352, 452
Sun, H., Li, Y.-P., Pan, Z., & Yang, H. 2026, Phys. Rev. D, 114, 023010
Syer, D., Clarke, C. J., & Rees, M. J. 1991, MNRAS, 250, 505
Tremaine, S., Richstone, D. O., Byun, Y.-I., et al. 1994, AJ, 107, 634
Vasiliev, E. 2017, ApJ, 848, 10
Vasiliev, E., & Merritt, D. 2013, ApJ, 774, 87
Wevers, T., Pasham, D. R., Jalan, P., Rakshit, S., & Arcodia, R. 2022, A&A, 659, L2
Xian, J., Zhang, F., Dou, L., He, J., & Shu, X. 2021, ApJ, 921, L32
Zhang, F., & Amaro Seoane, P. 2026, ApJ, 999, 224
Zhou, C., Zhong, B., Zeng, Y., Huang, L., & Pan, Z. 2024, Phys. Rev. D, 110, 083019

Table A.1. QPE selection factor $\mu^{T,e,i} = N_{CO}/N^{tot}_{\rm EMRI}$ for different values of the maximum period $T_{\rm QPE}$, and the maximum eccentricity $e^{\rm max}_{\rm QPE}$ compatible with QPEs. We consider NSCs with central MBH of mass $M_\bullet$ and EMRIs from COs of different mass $M_{\rm CO}$. For sBHs ($M_{\rm CO} = 10, 40\,M_\odot$) $\mu^{T,e,i}$ also accounts for inclination constraints $0° < i < 20°$. "-" means that the period at $r_{\rm cap}$ is longer than $T_{\rm QPE}$.

		$M_\bullet$																				
		$10^5\,M_\odot$			$3\times10^5\,M_\odot$			$10^6\,M_\odot$			$3\times10^6\,M_\odot$			$10^7\,M_\odot$			$3\times10^7\,M_\odot$			$10^8\,M_\odot$		
		$M_{\rm CO}$			$M_{\rm CO}$			$M_{\rm CO}$			$M_{\rm CO}$			$M_{\rm CO}$			$M_{\rm CO}$			$M_{\rm CO}$		
		$10\,M_\odot$	$40\,M_\odot$	$1\,M_\odot$	$10\,M_\odot$	$40\,M_\odot$	$1\,M_\odot$	$10\,M_\odot$	$40\,M_\odot$	$1\,M_\odot$	$10\,M_\odot$	$40\,M_\odot$	$1\,M_\odot$	$10\,M_\odot$	$40\,M_\odot$	$1\,M_\odot$	$10\,M_\odot$	$40\,M_\odot$	$1\,M_\odot$	$10\,M_\odot$	$40\,M_\odot$	$1\,M_\odot$
$T_{\rm QPE}$	$e^{\rm max}_{\rm QPE}$																					
48 h	0.05	1.6×10^{-6}	3.9×10^{-6}	0.0	2.3×10^{-6}	5.7×10^{-6}	0.0	3.3×10^{-6}	8.2×10^{-6}	3.1×10^{-6}	4.8×10^{-6}	1.2×10^{-5}	6.1×10^{-5}	6.7×10^{-6}	1.6×10^{-5}	1.4×10^{-4}	8.8×10^{-6}	1.4×10^{-5}	2.52×10^{-4}	1.3×10^{-5}	6.4×10^{-6}	4.4×10^{-4}
	0.2	5.6×10^{-5}	1.3×10^{-4}	0.0	8.1×10^{-5}	2.0×10^{-4}	0.0012	1.1×10^{-4}	2.8×10^{-4}	0.0035	1.6×10^{-4}	3.0×10^{-4}	0.0051	1.7×10^{-4}	1.8×10^{-4}	0.0061	1.0×10^{-4}	7.1×10^{-5}	0.0073	7.7×10^{-5}	3.6×10^{-5}	0.0036
	1	0.0074	0.0083	1.0	0.0057	0.0056	0.75	0.0040	0.0031	0.47	0.0024	0.0014	0.26	0.0012	5.5×10^{-4}	0.13	4.6×10^{-4}	1.6×10^{-4}	0.056	3.2×10^{-4}	1.5×10^{-4}	0.013
20 h	0.05	1.6×10^{-6}	3.9×10^{-6}	0.0	2.3×10^{-6}	5.7×10^{-6}	0.0	3.3×10^{-6}	8.2×10^{-6}	3.1×10^{-6}	4.8×10^{-6}	1.1×10^{-5}	6.1×10^{-5}	6.5×10^{-6}	9.5×10^{-6}	1.4×10^{-4}	5.0×10^{-6}	4.4×10^{-6}	2.47×10^{-4}	4.3×10^{-6}	2.0×10^{-6}	1.9×10^{-4}
	0.2	5.6×10^{-5}	1.3×10^{-4}	0.0	8.1×10^{-5}	1.9×10^{-4}	0.0012	1.1×10^{-4}	1.9×10^{-4}	0.0035	1.1×10^{-4}	1.1×10^{-4}	0.0051	7.1×10^{-5}	4.6×10^{-5}	0.0052	3.4×10^{-5}	1.5×10^{-5}	0.0032	2.3×10^{-5}	1.1×10^{-5}	0.0011
	1	0.0039	0.0036	0.49	0.0026	0.0020	0.34	0.0015	9.2×10^{-4}	0.20	8.1×10^{-4}	3.6×10^{-4}	0.099	3.5×10^{-4}	1.2×10^{-4}	0.041	1.1×10^{-4}	2.9×10^{-5}	0.015	7.4×10^{-5}	3.3×10^{-5}	0.0025
9 h	0.05	1.6×10^{-6}	3.9×10^{-6}	0.0	2.3×10^{-6}	5.7×10^{-6}	0.0	3.3×10^{-6}	7.9×10^{-6}	3.1×10^{-6}	4.5×10^{-6}	6.4×10^{-6}	6.1×10^{-5}	3.8×10^{-6}	3.2×10^{-6}	1.4×10^{-4}	2.0×10^{-6}	1.2×10^{-6}	1.5×10^{-4}	-	-	-
	0.2	5.6×10^{-5}	1.3×10^{-4}	0.0	7.9×10^{-5}	1.3×10^{-4}	0.0012	7.6×10^{-5}	7.2×10^{-5}	0.0035	5.0×10^{-5}	3.2×10^{-5}	0.0044	2.6×10^{-5}	1.2×10^{-5}	0.0025	1.1×10^{-5}	3.3×10^{-6}	0.0012	-	-	-
	1	0.0019	0.0014	0.15	0.0011	6.7×10^{-4}	0.12	5.8×10^{-4}	2.6×10^{-4}	0.067	2.7×10^{-4}	9.2×10^{-5}	0.030	9.9×10^{-5}	2.6×10^{-5}	0.011	2.5×10^{-5}	5.2×10^{-6}	0.0038	-	-	-
2 h	0.05	1.6×10^{-6}	3.7×10^{-6}	0.0	2.2×10^{-6}	3.2×10^{-6}	0.0	1.9×10^{-6}	1.7×10^{-6}	3.1×10^{-6}	1.2×10^{-6}	7.2×10^{-7}	2.9×10^{-5}	6.2×10^{-7}	2.6×10^{-7}	2.1×10^{-5}	-	-	-	-	-	-
	0.2	3.9×10^{-5}	3.9×10^{-5}	0.0	2.7×10^{-5}	1.9×10^{-5}	3.5×10^{-4}	1.5×10^{-5}	7.3×10^{-6}	4.4×10^{-4}	7.4×10^{-6}	2.6×10^{-6}	2.5×10^{-4}	3.0×10^{-6}	7.3×10^{-7}	1.0×10^{-4}	-	-	-	-	-	-
	1	3.7×10^{-4}	1.7×10^{-4}	0.0	1.8×10^{-4}	6.4×10^{-4}	3.8×10^{-4}	7.4×10^{-5}	2.1×10^{-5}	4.5×10^{-4}	2.6×10^{-5}	5.7×10^{-6}	2.6×10^{-4}	6.0×10^{-6}	1.1×10^{-6}	1.0×10^{-4}	-	-	-	-	-	-

Table A.2. Average number of active QPEs $\langle N_{\rm QPE}\rangle$ over 10 Gyr, as estimated from two-body relaxation simulations. We use the same symbols as in Table A.1. At each snapshot of the simulation, we compute $N_{\rm QPE} = N_{\rm disks}\,N_{\rm CO}$ as explained in Sect. 4. "-" means that the period at $r_{\rm cap}$ is longer than $T_{\rm QPE}$.

		$M_\bullet$																				
		$10^5\,M_\odot$			$3\times10^5\,M_\odot$			$10^6\,M_\odot$			$3\times10^6\,M_\odot$			$10^7\,M_\odot$			$3\times10^7\,M_\odot$			$10^8\,M_\odot$		
		$M_{\rm CO}$			$M_{\rm CO}$			$M_{\rm CO}$			$M_{\rm CO}$			$M_{\rm CO}$			$M_{\rm CO}$			$M_{\rm CO}$		
		$10\,M_\odot$	$40\,M_\odot$	$1\,M_\odot$	$10\,M_\odot$	$40\,M_\odot$	$1\,M_\odot$	$10\,M_\odot$	$40\,M_\odot$	$1\,M_\odot$	$10\,M_\odot$	$40\,M_\odot$	$1\,M_\odot$	$10\,M_\odot$	$40\,M_\odot$	$1\,M_\odot$	$10\,M_\odot$	$40\,M_\odot$	$1\,M_\odot$	$10\,M_\odot$	$40\,M_\odot$	$1\,M_\odot$
$T_{\rm QPE}$	$e^{\rm max}_{\rm QPE}$																					
48 h	0.05	5.0×10^{-14}	10^{-12}	0.0	6.0×10^{-13}	1.2×10^{-11}	0.0	6.6×10^{-12}	1.3×10^{-10}	1.1×10^{-11}	6.6×10^{-11}	1.2×10^{-9}	10^{-10}	8.6×10^{-10}	1.4×10^{-8}	4.2×10^{-7}	4.3×10^{-9}	3.4×10^{-8}	3.7×10^{-6}	6.7×10^{-10}	2.3×10^{-10}	7.4×10^{-6}
	0.2	1.7×10^{-12}	3.5×10^{-11}	0.0	2.1×10^{-11}	4.2×10^{-10}	1.8×10^{-10}	2.3×10^{-10}	4.5×10^{-9}	3.6×10^{-8}	2.3×10^{-9}	3.5×10^{-8}	10^{-6}	2.2×10^{-8}	1.6×10^{-7}	1.8×10^{-5}	5.0×10^{-8}	1.7×10^{-7}	10^{-4}	4.0×10^{-9}	1.3×10^{-9}	6.0×10^{-5}
	1	2.8×10^{-10}	2.9×10^{-9}	3.5×10^{-9}	1.9×10^{-9}	1.6×10^{-8}	4.0×10^{-7}	9.5×10^{-9}	6.5×10^{-8}	7.4×10^{-6}	3.8×10^{-8}	1.8×10^{-7}	6.1×10^{-5}	1.5×10^{-7}	4.9×10^{-7}	3.8×10^{-4}	2.2×10^{-7}	3.4×10^{-7}	8.2×10^{-4}	1.6×10^{-8}	5.4×10^{-9}	2.2×10^{-4}
20 h	0.05	5.0×10^{-14}	10^{-12}	0.0	6.0×10^{-13}	1.2×10^{-11}	0.0	6.6×10^{-12}	1.3×10^{-10}	1.1×10^{-11}	6.6×10^{-11}	1.2×10^{-10}	9.9×10^{-9}	8.2×10^{-10}	8.4×10^{-9}	4.2×10^{-7}	2.4×10^{-9}	1.1×10^{-8}	3.6×10^{-6}	2.2×10^{-10}	7.3×10^{-11}	3.1×10^{-6}
	0.2	1.7×10^{-12}	3.5×10^{-11}	0.0	2.1×10^{-11}	4.2×10^{-10}	1.8×10^{-10}	2.2×10^{-10}	3.5×10^{-9}	3.6×10^{-8}	1.7×10^{-9}	1.3×10^{-8}	10^{-6}	9.1×10^{-9}	4.1×10^{-8}	1.6×10^{-5}	1.6×10^{-8}	3.7×10^{-8}	4.7×10^{-5}	1.2×10^{-9}	4.0×10^{-10}	1.9×10^{-5}
	1	1.6×10^{-10}	1.3×10^{-9}	1.3×10^{-9}	9.0×10^{-10}	6.2×10^{-9}	1.8×10^{-7}	3.9×10^{-9}	1.9×10^{-8}	3.2×10^{-6}	1.3×10^{-8}	4.5×10^{-8}	2.3×10^{-5}	4.4×10^{-8}	1.0×10^{-7}	1.2×10^{-4}	5.3×10^{-8}	7.0×10^{-8}	2.2×10^{-4}	3.8×10^{-9}	1.2×10^{-9}	4.3×10^{-5}
9 h	0.05	5.0×10^{-14}	10^{-12}	0.0	6.0×10^{-13}	1.2×10^{-11}	0.0	6.6×10^{-12}	1.3×10^{-10}	1.1×10^{-11}	6.4×10^{-11}	7.7×10^{-10}	9.9×10^{-9}	4.8×10^{-10}	2.8×10^{-9}	4.2×10^{-7}	9.8×10^{-10}	2.9×10^{-9}	2.1×10^{-6}	-	-	-
	0.2	1.7×10^{-12}	3.5×10^{-11}	0.0	2.1×10^{-11}	3.4×10^{-10}	1.8×10^{-10}	1.8×10^{-10}	1.5×10^{-9}	3.6×10^{-8}	7.9×10^{-10}	4.0×10^{-9}	9.4×10^{-7}	3.3×10^{-9}	10^{-8}	7.5×10^{-6}	5.2×10^{-9}	8.1×10^{-9}	1.8×10^{-5}	-	-	-
	1	8.2×10^{-11}	5.6×10^{-10}	3.4×10^{-10}	4.1×10^{-10}	2.1×10^{-9}	6.1×10^{-8}	1.5×10^{-9}	5.7×10^{-9}	1.1×10^{-6}	4.3×10^{-9}	1.1×10^{-8}	7.1×10^{-6}	1.2×10^{-8}	2.3×10^{-8}	3.4×10^{-5}	1.2×10^{-8}	1.3×10^{-8}	5.5×10^{-5}	-	-	-
2 h	0.05	5.0×10^{-14}	10^{-12}	0.0	6.0×10^{-13}	9.0×10^{-12}	0.0	4.6×10^{-12}	3.6×10^{-11}	1.1×10^{-11}	1.9×10^{-11}	9.1×10^{-11}	5.6×10^{-9}	7.9×10^{-11}	2.3×10^{-10}	6.3×10^{-8}	-	-	-	-	-	-
	0.2	1.5×10^{-12}	1.5×10^{-11}	0.0	9.6×10^{-12}	6.0×10^{-11}	6.1×10^{-11}	3.8×10^{-11}	1.6×10^{-10}	6.2×10^{-9}	1.2×10^{-10}	3.2×10^{-10}	6.0×10^{-8}	3.9×10^{-10}	6.5×10^{-10}	3.1×10^{-7}	-	-	-	-	-	-
	1	1.7×10^{-11}	7.3×10^{-11}	0.0	6.6×10^{-11}	2.1×10^{-10}	6.8×10^{-11}	1.9×10^{-10}	4.5×10^{-10}	6.4×10^{-9}	4.0×10^{-10}	6.8×10^{-10}	6.1×10^{-8}	7.6×10^{-10}	9.6×10^{-10}	3.1×10^{-7}	-	-	-	-	-	-